RESEARCH ACTIVITIES

Photo-Molecular Science

We study the interaction between molecules and optical fields with its possible applications to active control of molecular functionality and reactivity. We also develop novel light sources to promote those studies. Two research facilities, the Laser Research Center for Molecular Science and the UVSOR, closely collaborate with the Department.

The core topics of the Department include ultrahigh-precision coherent control of gas- and condensed-phase molecules, high-resolution optical microscopy applied to nanomaterials, synchrotron-based spectroscopy of core-excited molecules and solid-state materials, vacuum-UV photochemistry, and the development of novel laser- and synchrotron-radiation sources.

Development of Advanced Near-Field Spectroscopy and Application to Nanometric Systems

Department of Photo-Molecular Science
Division of Photo-Molecular Science I

OKAMOTO, Hiromi	Professor
NARUSHIMA, Tetsuya	Assistant Professor
NISHIYAMA, Yoshio	IMS Research Assistant Professor
KOWAKA, Yasuyuki	Post-Doctoral Fellow
WU, Huijun	Graduate Student (–March, 2012) Technical Fellow (April, 2012–)
HASHIYADA, Shun	Graduate Student
OCHIAI, Takao	Graduate Student*
ISHIKAWA, Akiko	Technical Fellow
NOMURA, Emiko	Secretary
YAMASAKI, Yumi	Secretary

There is much demand for the study of local optical properties of molecular assemblies and materials, to understand nanoscale physical and chemical phenomena and/or to construct nanoscale optoelectronic devices. Scanning near-field optical microscopy (SNOM) is an imaging method that enables spatial resolution beyond the diffraction limit of light. Combination of this technique with various advanced spectroscopic methods may offer a direct probe for dynamics in nanomaterials and nanoscale functionalities. It may provide essential and basic knowledge to analyze origins of characteristic features of the nanomaterial systems. We have constructed apparatuses of near-field spectroscopy and microscopy for excited-state studies of nanomaterials, with the feasibilities of nonlinear and time-resolved measurements. The developed apparatuses enable near-field measurements of two-photon induced emission and femtosecond time-resolved signals, in addition to conventional transmission, emission, and Raman scattering. Based on these methods, we are investigating the characteristic spatiotemporal behaviors of various metal-nanoparticle systems and molecular assemblies.

1. Visualization of Localized Optical Fields and Plasmon Wavefunctions in Metal Nanostructures

We recently reported that wavefunctions of localized plasmon resonances of chemically synthesized metal (Au and Ag) nanoparticles are visualized by near-field transmission or two-photon excitation measurements.[1)] The same methods were also applied to Au nanoparticle assemblies to visualize confined optical fields.[1)] It was revealed for the Au nanoparticle dimers that highly localized optical field is generated at the interstitial sites between the particles. In many-particle assemblies, the localized fields were especially intensified at the rim parts of the assemblies, and such a characteristic field distribution has been attributed to interaction between plasmon excitations induced on the particles. We also observed confined optical fields in gaps between circular apertures opened on thin gold films.

We are extending the studies to various two-dimensional metal nanostructures manufactured by the electron-beam lithography technique, in part as collaboration with researchers of other institution, with which structures that are difficult to obtain with the chemical methods can be available. The nanostructures now under study are circular Au nanodisks, assembled Au nanodisks with designed arrangements, elongated rectangular nanoapertures opened on Au thin films, and so forth. Such a study is essential as a basis for designing unique optical properties and functions of metal nanostructures.

2. Studies of Metal-Nanostructure Modified Photovoltaic Cells by Near-Field Excited Site-Specific Photocurrent Detection

Metal nanoparticles and their assemblies collect photon energies to yield confined and enhanced optical fields in the vicinities of the particles due to plasmon resonances. Recently, it has been reported that efficiencies of photoenergy conversion can be improved by the use of noble metal nanostructures. The photoenergy conversion system ranges from wet-type and solid-state photo-current conversion cells to photo-chemical conversion systems. To reveal the mechanism of the enhanced photoenergy conversion process, studies of detailed nanostructures and site-dependent photocurrent measurements are essential.

We applied SNOM to clarify effects of surface plasmon resonance on photo-current conversion in GaAs semiconductor cells modified with Au nanoparticles, by photocurrent imaging measurements with localized near-field photoirradiation (Figure 1).[2)] Isolated nanospheres caused local photocurrent sup-

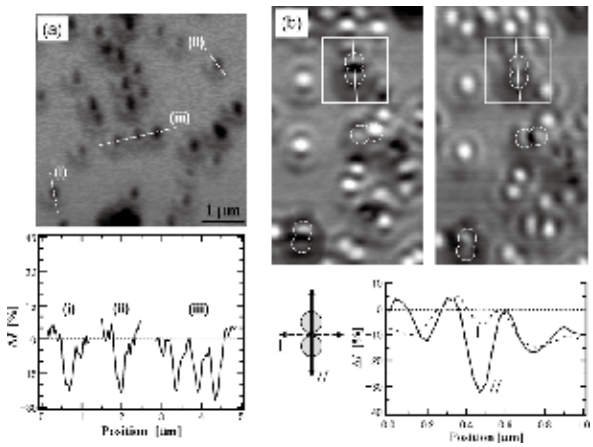

Figure 1. Near-field photocurrent images for GaAs photodiode modified with Au spherical nanoparticles. (a) Phorocurrent image at 532 nm for isolated particles (top) and line profiles along the dashed lines in the image (bottom). (b) Photocurrent images at 785 nm for dimeric particles (top; dimers are indicated with white circles; vertical and horizontal polarizations for left and right images, respectively) and line profiles along the white lines in the image for respective polarization directions (bottom).

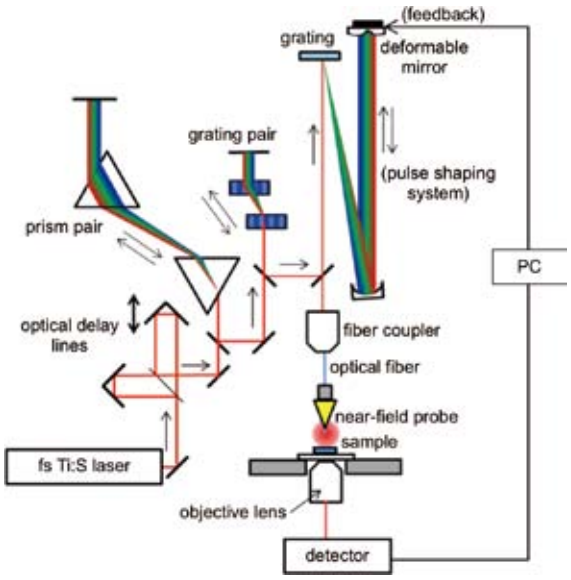

Figure 2. Experimental setup of sub-20-fs ultrafast near-field measurement.

pressions at the plasmon resonance wavelengths (~530 nm). In assemblies (dimers and trimers) of the spheres, a remarkable decrease of photocurrent at the gap site between the spheres was observed at ~800 nm near the dimer plasmon resonance, despite anticipated field enhancements in the gap sites. From the results, it is concluded that the enhanced optical fields induced by the plasmons do not improve the photovoltaic efficiency. The far-field forward scattering of photons by the gold nanoparticles may be more important than the enhanced field effects for the GaAs photovoltaic device studied.

3. Construction of Apparatuses for Sub-20-fs Ultrafast Near-Field Spectroscopy

Surface plasmons of noble metal nanoparticles have very short lifetimes in the range of ~2–20 fs. To achieve a SNOM observation of such fast dynamics in the individual nanoparticles, we have to overcome serious dispersion effects arising from the optical components involved, especially from the optical fiber. We achieved that by combining the conventional dispersion compensation devices composed of prism and grating pairs with adaptive pulse shaping technique, and succeeded in delivering 17-fs pulses to the the near-field aperture with a spatial resolution of ~100 nm.[3)]

The layout of the experimental setup is shown in Figure 2. A pair of transmission gratings and an SF14 prism pair were adopted to precompensate for the second- and third-order group velocity dispersion effects. The beam was then sent to adaptive pulse shaping system equipped with a deformable mirror, whose surface shape was adjusted to yield a shortest pulse duration at the probe tip using a genetic algorithm. The laser beam was then coupled to a 150-mm-long optical fiber to introduce the light into the apertured near-field probe tip. We used time-correlated two-photon-induced photoluminescence (TPI-PL) measurements to demonstrate the performance of the system. The light pulses were incident on a gold nanostructure sample through the near-field probe to excite the TPI-PL from Au, whose intensity was recorded as a function of the pump–probe delay time. With this setup we succeeded in measuring dephasing of ~10 fs in Au nanostructures. Position dependent dephasing measurements for Au nanostructures are now under way.

4. Near-Field Circular Dichroism Microscopy of Nanomaterials

Circular dichroism (CD) spectroscopy is widely used in the studies of chiral materials and magnetism. Some of nanomaterials composed of achiral molecules are reported to show CD activities arising from the nanoscale chirality. Two-dimensionally chiral metal nanostructures also show CD activities. Investigation of nanoscale local CD may provide valuable information on the origins of CD activities of such materials. For this purpose, we are developing an apparatus for near-field CD microscopy and measuring CD images of nanoscale chiral materials.

References

1) H. Okamoto and K. Imura, *Prog. Surf. Sci.* **84**, 199–229 (2009).
2) Y. Harada, K. Imura, H. Okamoto, Y. Nishijima, K. Ueno and H. Misawa, *J. Appl. Phys.* **110**, 104306 (2011).
3) H. J. Wu, Y. Nishiyama, T. Narushima, K. Imura and H. Okamoto *Appl. Phys. Express* **5**, 062002 (2012).

* carrying out graduate research on Cooperative Education Program of IMS with University of Tsukuba

Design and Reconstruction of Molecular Quantum States of Motion

Department of Photo-Molecular Science
Division of Photo-Molecular Science I

OHSHIMA, Yasuhiro	Professor
MIZUSE, Kenta	Assistant Professor
FUJIWARA, Masanori	IMS Research Assistant Professor
HAYASHI, Masato	Post-Doctoral Fellow
MIYAKE, Shinichiro	Graduate Student
INAGAKI, Itsuko	Secretary

Molecules are vital existence. In a gas-phase ensemble at room temperature, they are, in an average, flying away by a few hundred meters, making turns almost reaching to 10^{11} times, and shaking themselves more than 10^{13} times within the duration of only one second. The ultimate goal this research group has been aiming to is to capture the lively figures of molecules moving in such a dynamic manner and to have a perfect command over the molecular motions. Here lasers with ultimate resolution in time and energy domains are employed complementally and cooperatively for this purpose.

1. Nonadiabatic Excitation of Molecular Rotation Induced by Intense Ultrashort Laser Fields

When a gaseous molecular sample is irradiated by an intense nonresonant ultrashort laser pulse, the laser field exerts a torque that aligns the molecular axis along the laser polarization vector, due to the interaction with the molecular anisotropic polarizability. Here the field–matter interaction only remains in much shorter duration than the characteristic time for molecular rotation, and thus the rotation of the molecules is coherently excited to create a rotational quantum wave packet (WP). We have developed a method to explore the nonadiabatic excitation in a quantum-state resolved manner and applied it to diatomic and symmetric-top molecules.[1)] It has been shown that the state distribution is a useful experimental source for verifying the excitation process.[2,3)] When a pair of excitation pulses is implemented with appropriate time delay between them, partial control of rotational-state distribution has been achieved.[1,4)] In a favorable case, the double-pulse excitation coupled with the state-selective probe has enabled us to reconstruct experimentally a rotational WP thus created.[5)] If the mutual polarization direction and time delay between the two pulses are adjusted, the sense of rotation around the laser propagation direction can also be controlled, yielding to a rotational WP exhibiting angular-momentum orientation.[6,7)]

2. Coherent Excitation of Intermolecular Vibrations in Molecular Clusters by Nonresonant Intense Ultrashort Laser Fields

Nonadiabatic interaction with a nonresonant intense ultrashort laser field can also coherently excite vibration of molecule through the structural dependence of the molecular polarizability. We have recently succeeded in creating and observing WPs pertinent to intermolecular vibrations of several molecular clusters in their electronic ground states. So far, NO–Ar, benzene dimer and trimer have been studied. Here, vibrational distribution after nonadiabatic vibrational excitation (NAVEX) is probed in a quantum-state resolved manner. By monitoring the resonant two-photon ionization (R2PI) spectra, substantial decrease of the transition from the vibrationally ground state has been clearly observed when the femtosecond (fs) pump pulse was applied, and in the case of NO–Ar, the observation was accompanied with the emergence of several hot bands, assigned to those from vibrationally excited states pertinent to intermolecular modes. The double fs pulse excitation has also been implemented for examining the real-time quantum interference of the WPs. The observed time-domain signals for NO–Ar were directly compared with the calculation on the WP propagation by numerically solving the time-dependent Schrödinger equation on the intermolecular potential energy surface. For more detailed examination of the NAVEX process and further application to various molecular cluster systems, we are now renovating the experimental setup, in particular, the molecular beam time-of-flight mass spectrometry (TOF-MS) apparatus. The modification includes: Improvement of mass resolution by extending the TOF flight tube, rejection of the interference of strong monomer signals by implementing a mass gate, and realization of more extensive cooling by enlarging the vacuum pumping capabilities.

3. High-Resolution Laser Spectroscopy of Benzene Clusters with Atoms and Small Molecules

Molecular clusters containing benzene are prototypical systems for elucidating the intermolecular interaction pertinent to aromatic rings. The information on the precise cluster geometry and energy-level structure pertinent to the intermolecular vibration are useful experimental input to reconstruct the intermolecular potential energy surface. We are now focusing on clusters of benzene attached by small numbers of atoms and molecules. So far, electronic spectra of C_6H_6 complexed with one and two He atom(s), two Ar atoms, up to three H_2 molecules, and one H_2O molecule have been examined via two-color R2PI in the vicinity of the monomer S_1–S_0 6_0^1 band. We employed a tripled output from a ns pulsed dye amplifier, which was injection-seeded by the CW output from a Ti:Sapphire laser, as an excitation source. Owing to the narrow band width (~250 MHz) of the laser system and the efficient rotational cooling down to 0.3 K by implementing a high-pressure pulsed valve, rotational structures have been greatly simplified.

Structural parameters of the clusters with He have been substantially refined than those reported previously.[8] The distances of He above the plane are set to be: 3.602 (+0.063) Å and 3.596 (+0.057) Å, respectively, for the clusters with one and two He atoms, where values in parentheses represent the change by the excitation from S_0 to S_1. Several vibronic bands with excitation of intermolecular vibrations have also been observed. The vibrational frequencies of benzene(S_1)–He are derived as: 17 and 13 cm^{-1} for the intermolecular stretch and bend modes, respectively. The intermolecular stretch of the cluster with two He is 15.72 cm^{-1}, while no experimental information has been obtained for the bend modes. The vibronic bands of benzene–He exhibit tunneling splitting due to a large-amplitude migration of He above and below the benzene molecular plane. This finding is matched with the prediction based on a high-level *ab initio* calculation. We have also recorded the R2PI spectrum of mono ^{13}C substituted species of benzene–He.

For the clusters with H_2, two distinguished isomers, correlating to *para* and *ortho* H_2, are identified. This finding shows that the permutation of the two H atoms in H_2 is feasible in the clusters. When the *normal* H_2 was used as a sample gas, only the clusters of *ortho* H_2 were observed, and thus we had to use a gas sample of pure *para* H_2 to record the clusters with *para* H_2 (see Figure 1). This observation indicates the smaller effective binding energy for benzene–*para* H_2 than that of the *ortho* H_2 cluster. This energy relation has been well known for the clusters with smaller molecules (*e.g.*, HF, HCl, and OCS) attached by H_2. It is noted the present study is the first experimental report on the coexistence of *para* and *ortho* H_2 isomers in the clusters of aromatic molecules. Rotationally resolved spectra allowed us to fix the cluster geometry unambiguously, as shown in Figure 2. It has shown that the effective intermolecular distances are substantially different from each other between the clusters with *para* and *ortho* H_2, indicating the change in the average H_2 orientation relative to the benzene plane in the two isomers.

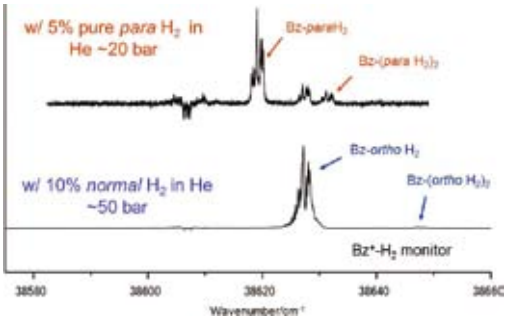

Figure 1. Excitation spectra of C_6H_6–$(H_2)_n$ recorded with the *normal* H_2 sample (bottom) and the pure *para* H_2 sample (top).

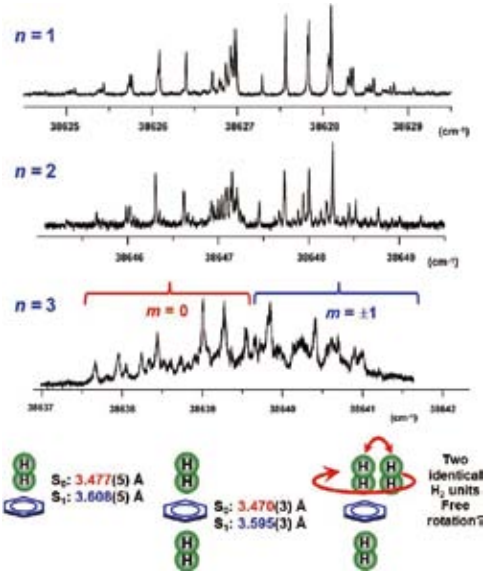

Figure 2. High-resolution excitation spectra and the experimentally derived cluster geometry of C_6H_6–(ortho $H_2)_n$.

We also recorded for the first time rotationally resolved excitation spectrum of the cluster with two Ar atoms lying on the same side of the benzene plane.

References

1) Y. Ohshima and H. Hasegawa, *Int. Rev. Chem. Phys.* **29**, 619–663 (2010).
2) H. Hasegawa and Y. Ohshima, *Phys. Rev. A* **74**, 061401 (4 pages) (2006).
3) H. Hasegawa and Y. Ohshima, *Chem. Phys. Lett.* **454**, 148–152 (2008).
4) D. Baek, H. Hasegawa and Y. Ohshima, *J. Chem. Phys.* **134**, 224302 (10 pages) (2011).
5) H. Hasegawa and Y. Ohshima, *Phys. Rev. Lett.* **101**, 053002 (4 pages) (2008).
6) K. Kitano, H. Hasegawa and Y. Ohshima, *Phys. Rev. Lett.* **103**, 223002 (4 pages) (2009).
7) Y. Khodorkovsky, K. Kitano, H. Hasegawa, Y. Ohshima and I. Sh. Averbukh, *Phys. Rev. A* **83**, 023423 (10 pages) (2011).
8) S, M. Beck, M. G. Liverman, D. L. Monts and R. E. Smalley, *J. Chem. Phys.* **70**, 232–237 (1979).

Development of High-Precision Coherent Control and Its Applications

Department of Photo-Molecular Science
Division of Photo-Molecular Science II

OHMORI, Kenji	Professor
KATSUKI, Hiroyuki	Assistant Professor
TAKEI, Nobuyuki	Assistant Professor
GOTO, Haruka	Post-Doctoral Fellow
SOMMER, Christian	Post-Doctoral Fellow
NAKAGAWA, Yoshihiro	Graduate Student
KOYASU, Kuniaki	Graduate Student
INAGAKI, Itsuko	Secretary
YAMAGAMI, Yukiko	Secretary

Coherent control is based on manipulation of quantum phases of wave functions. It is a basic scheme of controlling a variety of quantum systems from simple atoms to nanostructures with possible applications to novel quantum technologies such as bond-selective chemistry and quantum computation. Coherent control is thus currently one of the principal subjects of various fields of science and technology such as atomic and molecular physics, solid-state physics, quantum electronics, and information science and technology. One promising strategy to carry out coherent control is to use coherent light to modulate a matter wave with its optical phase. We have so far developed a high-precision wave-packet interferometry by stabilizing the relative quantum phase of the two molecular wave packets generated by a pair of femtosecond laser pulses on the attosecond time scale. We will apply our high-precision quantum interferometry to gas, liquid, solid, and surface systems to explore and control various quantum phenomena.

Award

OHMORI, Kenji; Humboldt Research Award (Germany).

Molecular Inner-Shell Spectroscopy: Local Electronic Structure and Intermolecular Interaction

Department of Photo-Molecular Science
Division of Photo-Molecular Science III

KOSUGI, Nobuhiro	Professor
YAMANE, Hiroyuki	Assistant Professor
NAGASAKA, Masanari	Assistant Professor
YUZAWA, Hayato	IMS Fellow
MOCHIZUKI, Kenji	Graduate Student
LELOUP, Valentin	Graduate Student*
NAKANE, Junko	Secretary

In order to reveal local electronic structures and weak intermolecular interactions in molecular systems such as organic solids, liquids, aqueous solutions, and molecular clusters, we are developing and improving several kinds of soft X-ray spectroscopic techniques, such as X-ray photoelectron spectroscopy (X-ray PES, XPS), X-ray absorption spectroscopy (XAS), resonant Auger electron spectroscopy (RAS), X-ray emission spectroscopy (XES), resonant XES (RXES), and resonant inelastic X-ray scattering (RIXS), at UVSOR in-vacuum undulator beamlines BL-3U and BL-6U with some international collaboration programs, and also an original *ab initio* quantum chemical program package GSCF, which is optimized to calculation of molecular inner-shell processes.

1. Concentration Dependence of Local Structure in Methanol-Water Binary Liquid

A water molecule has two H(hydrogen)-accepting ('acceptor') and H-donating ('donor') sites, and the water liquid forms three dimensional (3D) hydrogen bonding (HB) networks. On the other hand, a methanol molecule with a hydrophobic methyl group has one H-donor and one or two H-acceptor sites, and the methanol liquid forms one and two dimensional (1D, 2D) HB networks, such as chains and rings of 6–8 methanol molecules. It is known that the methanol–water binary liquid has 3D cluster structures. However, the local structures of the methanol–water mixtures are still unknown. In this work, the local structure of the methanol–water binary liquid at different concentrations is studied by using carbon K-edge XAS.

The experiments were performed at soft X-ray undulator beam line BL3U at UVSOR-II facility. The liquid thin layer was sandwiched between two 100 nm-thick Si_3N_4 membranes. The photon energy was calibrated by the first peak (287.96 eV) of methanol gas filled in a He buffer space between the Si_3N_4 membrane and the detector in the liquid cell.

Figure 1 shows the carbon K-edge XAS spectra of the methanol–water binary liquids. The peak around 288.5 eV arises from the molecular orbital with a component of the hydroxyl group in the methanol molecule, and has a HB effect. On the other hand, the peak around 290 eV is mainly distributed at the methyl group. This peak is shifted to the higher photon energy by increasing the mixing ratio of water. It means that the methyl groups approach with each other in a dilute aqueous solution and the interaction between the methyl groups increase, contrary to liquid methanol, where the methyl groups are apart from each other.

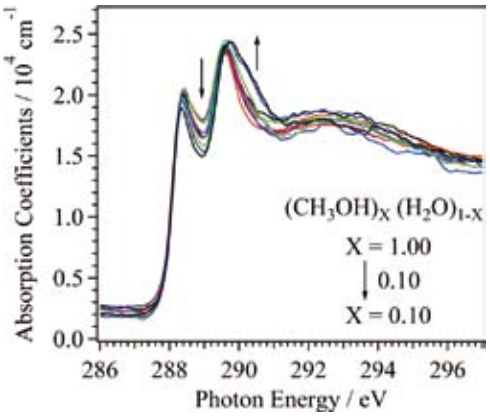

Figure 1. Carbon K-edge XAS spectra of the methanol-water binary liquid at different concentrations at 25 °C. The mixing ratio of water is increased along indicated arrows.

Figure 2 shows the intensities of the 289 eV region at different mixing ratios. The intensities are changed non-linearly, and indicate three different regions. The intensities are not changed so much in the methanol-rich region (I), indicating the local structure of pure methanol chain and ring clusters is preserved. On the other hand, in the region (II), the intensity is suddenly decreased at the methanol molar fraction $X \approx 0.7$, indicating a 1D/2D methanol–water mixed cluster is suddenly formed and this local structure is preserved down to $X \approx 0.3$. When $X <$ ~0.3 (III), the intensity is going down, indicating a 3D methanol–water mixed cluster is almost proportionally formed.

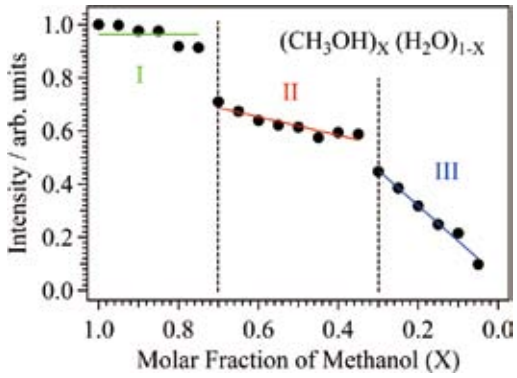

Figure 2. Intensities of the 289 eV region as a function of molar fraction of methanol in the methanol–water mixtures. The intensities of methanol and water are normalized to one and zero, respectively

2. Intramolecular and Intermolecular Interactions in Crystalline Films of Zinc Phthalocyanine (ZnPc)

It has been theoretically predicted that local and nonlocal electron–phonon (e–ph) interactions play a crucial role in the charge transport mechanism in organic solids. Recently, we have succeeded in observation of a small energy *versus* wave-vector [$E(\boldsymbol{k})$] relation for the crystalline film of an archetypal organic semiconductor of ZnPc on Au(111) by using the high-resolution angle-resolved UV photoemission spectroscopy (ARPES). Based on the precise $E(\boldsymbol{k})$ data, we have evaluated the e–ph interaction on the charge transport mechanism of the ZnPc crystalline film.

Figure 3(a) shows the $E(\boldsymbol{k})$ relation of the ZnPc crystalline film on Au(111), which is obtained from the photon energy dependence of the normal-emission ARPES spectra at 15 K. The highest occupied molecular orbital [HOMO (π, a_{1u})], Zn 3d (b_{1g}), and π's derived peaks show a dispersive shift with the same periodicity. This periodicity corresponds well with the highly symmetric Γ and Y points, estimated from the lattice constant of 3.32 Å determined by the specular X-ray diffraction [Figure 3(b)].

In order to examine the e–ph coupling in crystalline ZnPc film, we measured the temperature dependence of ARPES at the Γ and Y points with the 60 and 90 eV incident photons, respectively. As seen in Figure 3(c), the Γ-point HOMO energy shifts depending on the temperature, while the Y-point HOMO energy seems independent on the temperature. From the lineshape analysis, we found that both the HOMO bandwidth (*i.e.*, energy difference between the Γ-HOMO and Y-HOMO) and the Γ-HOMO peakwidth are narrowed with increasing the temperature, which is an opposite behavior to the remanent Au(111) Fermi edge. This is distinct indication of the local/nonlocal e–ph interaction; that is, band narrowing due to the interaction with local phonons (*intra*molecular vibrations) and band widening due to the interaction with nonlocal phonons (*inter*molecular lattice vibrations). Judging from the temperature dependence of the HOMO bandwidth and peakwidth, it is considered that the temperature-dependent transition between the incoherent hopping transport associated with the local e–ph coupling and the coherent band transport associated with the nonlocal e–ph coupling occurs within the energy scale of 100 meV in the ZnPc crystalline film.

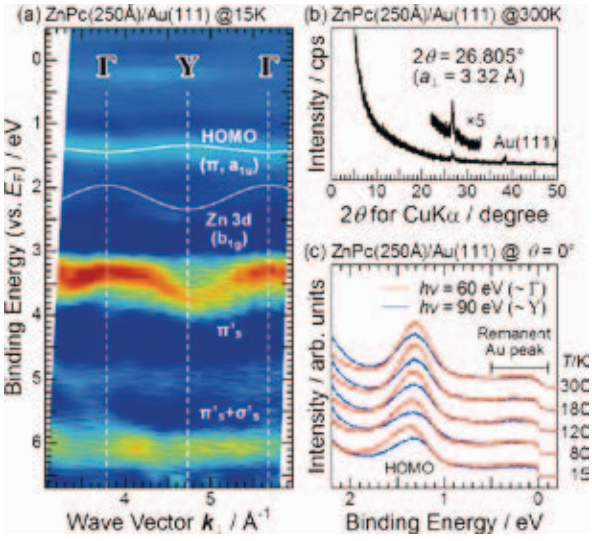

Figure 3. (a) Intermolecular $E(\boldsymbol{k})$ relation of the crystalline ZnPc film on Au(111) at 15 K, wherein the second derivative of the ARPES spectra were used for mapping out. White curves for the HOMO and Zn 3d derived bands are the best-fit results in the tight-binding model. (b) CuKα X-ray diffraction of the crystalline ZnPc film on Au(111) at 300 K. (c) Temperature dependence of ARPES in the HOMO-band region at the Γ and Y points, measured with 60 and 90 eV incident photons, respectively.

* carrying out graduate research on Cooperative Education Program of IMS with Ecole Nationale Superieure de Chimie de Paris

Photoabsorption and Photoionization Studies of Fullerenes and Development of High-Efficiency Organic Solar Cells

Department of Photo-Molecular Science
Division of Photo-Molecular Science III

MITSUKE, Koichiro	Associate Professor (–March, 2012)*
KATAYANAGI, Hideki	Assistant Professor
PRAJONGTAT, Pongthep	Research Fellow
MORENOS, Lei Angeli S.	Visiting Scientist
VAILIKHIT, Veeramol	Visiting Scientist
BASHYAL, Deepak	Graduate Student
ASARI, Chie	Technical Fellow
SHIMIZU, Atsuko	Secretary

We have observed the formation of multiply-charged photoions from gaseous fullerenes or aromatic hydrocarbons irradiated with synchrotron radiation at $h\nu$ = 25 to 200 eV. We thus studied the mechanisms and kinetics of consecutive C_2-release reactions on the basis of (i) the yield curves for the fragments $C_{60(70)-2n}^{z+}$ ($n \geq 1$, z = 1–3) as a function of the primary internal energy and (ii) the three dimensional velocity distributions of the fragments. The velocity distributions of C_{60-2n}^{z+} and C_{70-2n}^{z+} were measured for the first time. Concepts of the microcanonical temperature and Arrhenius-type rate constants for individual C_2 ejection steps allowed us to compare the experimental total average kinetic energy with theoretical kinetic energy release predicted from the "model free approach" developed by Klots.

In the second topic, we have fabricated dye-sensitized solar cells (DSSCs) containing ruthenium dye, iodide electrolyte, and platinum or carbon nanotube catalysts. The incidence photon-to-current conversion efficiencies (IPCE) and photoabsorbance (ABS) were measured in the range of 300 nm to 1 μm. We also evaluated the quantum yield (APCE) of DSSCs for the electron injection from the excited orbital of Ru dye to the conduction band of mesoporous TiO_2 nanoparticles. Our final goal is to develop DSSCs with high performance by improving ABS and APCE.

1. Photodissociation Dynamics of Fullerenes by Velocity Map Imaging with Improved Mass Resolution

We observed images of three-dimensional scattering velocity distributions of fragments produced by the photodissociation of the fullerenes, C_{60} and C_{70}, using a mass-resolved velocity map imaging spectrometer.[1,2] From the images we successfully obtained translational temperatures of the fragments and kinetic energy releases. Still the peaks of the fragments were found to be partially overlapped in their time-of-flight (TOF) mass spectra. We tried to improve the mass resolution of the imaging spectrometer by adding a focusing electrode to the Eppink-Parker type imaging electrode assembly.[3] This focusing electrode was designed after the ion lens device presented by Peši.

After introducing the focusing electrode, vertical stripes involving the fragment ions are completely resolved in the velocity vs. TOF maps, or y–t maps, and their masses are unquestionably identified. The y–t maps with improved mass resolution were obtained for C_{70} with the excitation photon energy $h\nu$ range of 70–125 eV. The translational temperature T_{trans} of each fragment was extracted from the map. The $h\nu$ dependence of T_{trans} exhibits the same propensity as that obtained previously[2] at low mass resolution. For C_{60}^{2+} from C_{70} singularity in T_{trans} remains also in the present measurements. Probably the C_{60}^{2+} formation mechanism is quite different from the stepwise C_2 emission from C_{70} that has widely been accepted for the other fragments.

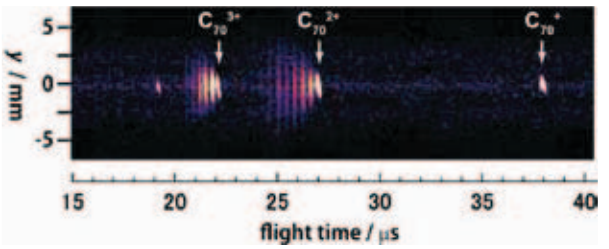

Figure 1. Y–t map of parent and fragment ions produced from C_{70} with the excitation $h\nu$ of 110 eV. The y coordinate is proportional to the y component of the ion velocity.

2. Estimation of the Translational Temperatures of High-Speed Fragment Ions Released from Sumanene and Coronene

Dissociative photoionization processes of polycyclic aromatic hydrocarbons (PAHs), sumanene $C_{21}H_{12}$ and coronene

$C_{24}H_{12}$, were studied by a mass-resolved velocity map imaging (VMI) technique. Since PAHs constitute the substructures of C_{60}, their behaviors in fragmentation are expected to have some analogies with those of fullerenes. Nevertheless, the *y–t* maps revealed a large difference in fragmentation mechanisms between PAHs and C_{60}. Main species produced from $C_{21}H_{12}$ and $C_{24}H_{12}$ were singly–charged ions with very high speed: CH^+, $C_2H_2^+$ and $C_nH_{n/2}^+$ ($2 < n < 13$). The translational energies of these fragments are so large that the scattering distributions extend beyond the coverage of our imaging apparatus. The peak profiles of the time-of-flight distributions were computer simulated on the basis of the ion trajectories calculated by the Simion–3D software. The translational temperatures of fragments from $C_{21}H_{12}$ were thus estimated to be 3000 to 30000 K (see Figure 2), depending on the number of carbon atoms in the fragments. A similar trend was observed for dissociation of $C_{24}H_{12}$. Our results suggest that dissociation of PAHs proceeds through the fission mechanism, which is not dominant in the fullerene cases.

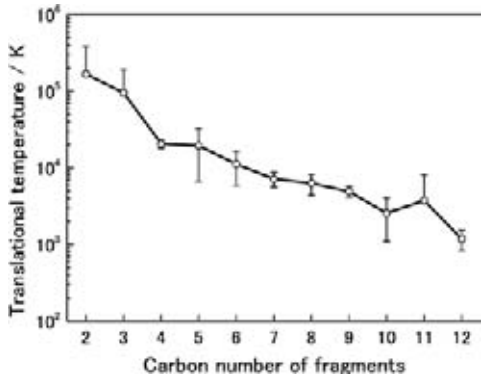

Figure 2. Translational temperatures of the fragment ions from coronene at *h*ν = 100 eV. Error bars show the standard deviations of repeated experimental runs.

3. Enhancement of the Solubility, Thermal Stability, and Electronic Properties of Carbon Nanotubes Functionalized by MEH-PPV

Multi-walled carbon nanotubes functionalized with poly [2-methoxy-5-(2'-ethylhexyloxy)-1,4-phenylenevinylene] (MWCNT-f-MEH-PPV) nanocomposites were successfully prepared by employing a "grafting from" approach.[4] The content of the functionalizing MEH-PPV in the composites was observed as 76%wt. Compared with pristine MWCNT, p-MWCNT, the aqueous solubility and thermal stability of the former are significantly enhanced. The effect of covalently and non-covalently functionalized nanotubes on the performances of the DSSCs has been investigated. The cells having the counter electrodes coated with isolated MEH-PPV, p-MWCNT/MEH-PPV, and MWCNT-f-MEH-PPV/MEH- PPV were fabricated. The cells based on a MWCNT- f-MEH-PPV/MEH-PPV counter electrode demonstrate the best photovoltaic performance as observed by higher J_{SC}, V_{OC}, and *FF* values. The experimental phenomena can be explained by quantum chemical calculations: Charge transfer from MEH-PPV oligomers to nanotubes is greater when covalently functionalized than when non-covalently functionalized. These suggest that the improvement in the photovoltaic parameters of the cells containing covalently functionalized nanotubes results not only from the higher concentration present in the nanotube films of the counter electrode, but also from the greater electron delocalization between the oligomers and nanotubes. The obtained results are very useful for enhancement of functionalized nanotubes applied to DSSCs.

4. Gas Phase Spectroscopy of Carbon Nanotubes

Our efforts have been concentrated on elucidation of the electronic and optical properties of fullerenes as well as their reaction dynamics in the gas phase. Such knowledge is critical in applying fullerenes to molecular functional devices. Recently, we started to investigate the properties of gaseous carbon nanotubes (CNTs) which of course form another group of promising carbon material.

CNTs are vaporized by matrix assisted laser desorption ionization (MALDI) and analyzed by time-of-flight (TOF) mass spectrometry. Commercially available multiwall CNT powder and single-wall CNT aqueous dispersion were used as samples. We have checked several solvents and matrices to optimize the MALDI conditions. The images of electron microscope prove that the laser irradiation certainly gives rise to vaporization of the sample. A temporal increase in the pressure of the sample chamber also supports the vaporization during the laser irradiation. Nevertheless, the signal of whole CNTs has not been observed yet. Smaller fragment ions C_n ($n < 200$) were only detected. Interaction between matrices and dispersants may prevent effective ionization.

We will continue to seek for the suitable vaporization method and construct a new vacuum chamber for the gas phase CNT experiment. The chamber will be connected to the beamline 4B in the UVSOR facility. Photoabsorption and photoionization experiments will be performed using the same chamber at the outset.

References

1) H. Katayanagi and K. Mitsuke, *J. Chem. Phys. (Communication)* **133**, 081101 (4 pages) (2010).
2) H. Katayanagi and K. Mitsuke, *J. Chem. Phys.* **135**, 144307 (8 pages) (2011).
3) K. Mitsuke, H. Katayanagi, B. Kafle and Md S. Prodhan, *ISRN Phys. Chem.* **2012**, 959074 (9 pages) (2012).
4) P. Prajongtat, S. Suramitr, M. P. Gleeson, K. Mitsuke and S. Hannongbua, *J. Mater. Sci.*, submitted.

* Present Position; Professor, Department of Chemistry, Faculty of Science, Josai University

Light Source Developments by Using Relativistic Electron Beams

UVSOR Facility
Division of Advanced Accelerator Research

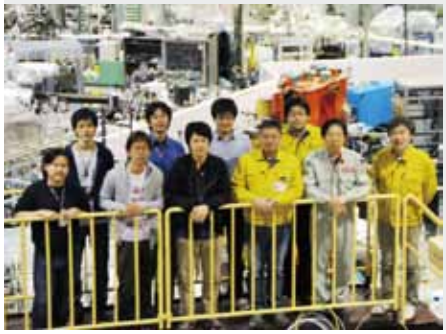

KATOH, Masahiro	Professor
ADACHI, Masahiro	Assistant Professor
KONOMI, Taro	Assistant Professor
OHIGASHI, Takuji	Assistant Professor
TANAKA, Seiichi	Post-Doctoral Fellow
ARAI, Hidemi	Post-Doctoral Fellow
TAIRA, Yoshitaka	Graduate Student*
GOTO, Yoshiaki	Graduate Student*
WASA, Naoki	Graduate Student*
HIDA, Yohei	Graduate Student*
UEMATSU, Youhei	Graduate Student*
NIWA, Takahiro	Graduate Student*

This project involves researches and developments on synchrotron light source, free electron laser, beam physics and their related technologies, including application of the light sources.

1. Developments on UVSOR Accelerators

The magnetic lattice of UVSOR was modified in 2012. This was the second major upgrade of the lattice, following the first one in 2003. This time all the bending (dipole) magnets were replaced with newly designed combined function ones. They have specially designed pole shapes and edge shapes as shown in Figure 1, to produce dipole, quadrupole and sextupole fields at the same time. By this modification, the emittance was reduced from 27 nm-rad to around 15 nm-rad, which would results in higher brightness of the synchrotron radiation. The magnetic lattice function changed, as shown in Figure 2. The storage ring was successfully commissioned in July with the new lattice. Fine machine tuning is in progress. After this upgrade, the ring is called UVSOR-III.

Figure 1. New combined function bending magnet (a lower half is shown).

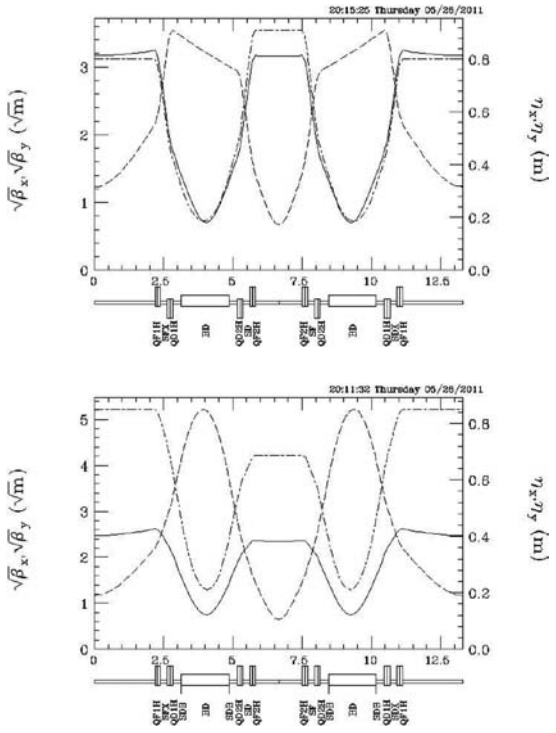

Figure 2. Lattice functions of UVSOR-II (upper) and UVSOR-III (lower). One quadrant of the ring is shown. The emittance is 27nm-rad and ~15nm-rad, respectively.

2. Construction of STXM Beam-Line

A new in-vacuum undulator was constructed and, in May 2012, it was installed at the last straight section in the ring reserved for insertion devices. This is the sixth undulator at UVSOR. It would provide soft X-rays to a scanning transmission X-ray microscope (STXM) beam-line.

Since April in 2012, the STXM beam-line, BL4U, has been constructed. Recently, its construction and installation of the STXM system were finished and their commissioning is due to start in October, 2012. We have been preparing the facilities of the beam-line, such as microscopes for pre-observations, a glove-box, an experimental hutch and infra-structures, for stating the operation in next April.

3. Light Source Developments

We have demonstrated that coherent synchrotron radiation of various properties could be generated in an electron storage ring by using an external laser source.[1–3] This research is supported by the Quantum Beam Technology Program of JST/MEXT. Under this support, a new experimental station has been constructed.[4] A new optical klystron/undulator was installed as shown in Figure 3. The magnetic field properties were verified by observing the spontaneous synchrotron radiation. The upgrade of the laser system was completed. The laser transport line, which was carefully designed as considering the effects of the air fluctuation, was also constructed. Two new beam-lines dedicated to the coherent lights in the VUV range and in the THz range has been almost completed.[5] The generation of coherent synchrotron radiation at the new site was successfully demonstrated. Some applications will be demonstrated soon in this fiscal year.

Figure 3. Experimental ser-up of Coherent Harmonic Generation at UVSOR-II.

A tunable, quasi-monochromatic ultra-short pulse and polarization-variable gamma-ray source is under development, based on a technology called Laser Compton scattering. The laser photons are Compton back-scattered by the high energy electrons and are converted to gamma-rays. The electron beam circulating in the storage ring is very thin in the vertical direction, typically in the order of 10 microns. By injecting laser light from the vertical direction to the beam, it is possible to produce ultra-short, quasi-monochromatic, energy tunable, polarization variable gamma-ray pulses. The energy tunability was successfully demonstrated.[6] An application utilizing the short pulse property was successfully demonstrated.

4. Accelerator Technology Developments

A novel beam injection scheme using a pulse sextupole magnet has been studied, in which the perturbation to the stored beam could be minimized during the injection. This is beneficial to the users experiments in the top-up operation mode. A new pulse sextupole magnet was designed and has been constructed. The field measurement is in progress. This device will be installed in the ring in September 2012.

A turn-by-turn beam position measurement system has been constructed, collaborating with the Equipment Development Center. This system enables to measure the electron beam orbit turn-by-turn just after the injection. It was proved that this device was a powerful tool for the commissioning of the storage ring.

References

1) (in alphabetic order) S. Bielawski, C. Evain, T. Hara, M. Hosaka, M. Katoh, S. Kimura, A. Mochihashi, M. Shimada, C. Szwaj, T. Takahashi and Y. Takashima, *Nat. Phys.* **4**, 390–393 (2008).
2) M. Labat, M. Hosaka, M. Shimada, M. Katoh and M. E. Couprie, *Phys. Rev. Lett.* **101**, 164803 (2008).
3) M. Shimada, M. Katoh, M. Adachi, T. Tanikawa, S. Kimura, M. Hosaka, N. Yamamoto, Y. Takashima and T. Takahashi, *Phys. Rev. Lett.* **103**, 144802 (2009).
4) M. Adachi, M. Katoh, H. Zen, T. Tanikawa, M. Hosaka, Y. Takashima, N. Yamamoto and Y. Taira, *AIP Conf. Proc.* **1234**, 492 (2010).
5) S. Kimura, E. Nakamura, M. Hosaka, T. Takahashi and M. Katoh, *AIP Conf. Proc.* **1234**, 63 (2010).
6) Y. Taira, M. Adachi, H. Zen, T. Tanikawa, M. Hosaka, Y. Takashima, N. Yamamoto, K. Soda and M. Katoh, *Nucl. Instrum. Methods Phys. Res., Sect. A* **637**, 5116–5119 (2011).

* carrying out graduate research on Cooperative Education Program of IMS with Nagoya University

Synchrotron Radiation Spectroscopy on Strongly Correlated Electron Systems

UVSOR Facility
Division of Advanced Solid State Physics

KIMURA, Shin-ichi	Associate Professor
MATSUNAMI, Masaharu	Assistant Professor
IMURA, Keiichiro	Post-Doctoral Fellow*
IIZUKA, Takuya	Graduate Student†
HAJIRI, Tetsuya	Graduate Student‡
NIWA, Ryosuke	Graduate Student‡
SHIMURA, Yusuke	Graduate Student‡
HIRATE, Satoshi	Graduate Student‡

Solids with strong electron–electron interaction, namely strongly correlated electron systems (SCES), have various physical properties, such as non-BCS superconducting, colossal magneto-resistance, heavy fermion and so on, which cannot be predicted by first-principle band structure calculation. Due to the physical properties, the materials are the candidates of the next generation functional materials. We investigate the mechanism of the physical properties as well as the electronic structure of SCES, especially rare-earth compounds, organic superconductors and transition-metal compounds, by infrared/THz spectroscopy and angle-resolved photoemission spectroscopy based on synchrotron radiation. Since experimental techniques using synchrotron radiation are evolved rapidly, the development of the synchrotron radiation instruments is also one of our research subjects.

1. Existence of Heavy Fermions in the Antiferromagnetic Phase of $CeIn_3$[1)]

Recently, physics at the quantum critical point (QCP), which is the border between local magnetism and itinerant paramagnetism at zero temperature, has become one of the main topics in the condensed-matter field because new quantum properties such as non-BCS superconductivity appear in the vicinity of the QCP. The ground state of rare-earth intermetallic compounds, namely, heavy-fermion (HF) materials, changes between the local magnetic and itinerant nonmagnetic states through external perturbation by such factors as pressure and magnetic field. The QCP appears owing to the energy balance between the local magnetic state based on the Ruderman–Kittel–Kasuya–Yoshida (RKKY) interaction and the itinerant HF state due to the Kondo effect. In the itinerant HF regime, the conduction band hybridizes with the nearly local 4*f* state, so that a large Fermi surface as well as the hybridization band between them, namely, the *c*–*f* hybridization band, is realized. In the case of a magnetic regime, on the other hand, two theoretical scenarios have been proposed. One is the spin-density wave (SDW) scenario based on spin fluctuation, in which large Fermi surfaces due to *c*–*f* hybridization remain even in magnetically ordered states. The other is the Kondo breakdown (KBD) scenario, in which the *c*–*f* hybridization state disappears in the magnetic state and only small Fermi surfaces due to conduction electrons appear. Many controversies for these scenarios have been performed so far, but the conclusion has not been obtained yet.

Here, we report the pressure-dependent electronic structure as well as the *c*–*f* hybridization state obtained by far-infrared reflectivity [$R(\omega)$] and optical conductivity [$\sigma(\omega)$] measurements of $CeIn_3$ under pressure. $CeIn_3$ has an AFM ground state with a Néel temperature T_N of 10 K. With the

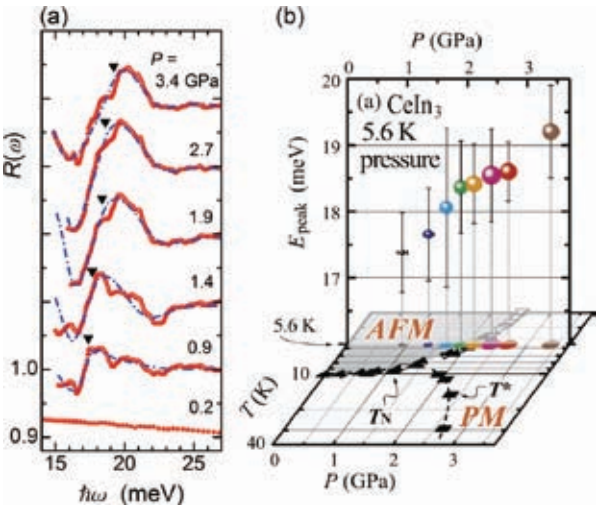

Figure 1. (a) Pressure dependence of the reflectivity [$R(\omega)$] spectrum (solid circles) of $CeIn_3$ and Drude-Lorentz fitting results (dotted-dashed lines) in the photon energy range of 14–27 meV at 5.6 K. The spectra are shifted by 0.1 for clarity. (b) The edges of $R(\omega)$ spectra as functions of pressure. The size of the marks denotes the intensity of the corresponding edge in the $R(\omega)$ spectra. The pressure-dependent Néel temperature (solid and open triangles, T_N) and valence transition temperature (solid squares, T^*) are also plotted at the bottom.

application of pressure, T_N monotonically decreases and disappears at a critical pressure of approximately 2.6 GPa. We observed that the *c–f* hybridization gap appears not only in the HF state but also in the AFM state, and both the energy and intensity of the σ(ω) peak due to the *c–f* hybridization band continuously increase with the application of pressure as shown in Figure 1. Our observations suggest that the electronic structure of $CeIn_3$ in the AFM phase can be explained by the SDW scenario because the *c–f* hybridization state exists even in the AFM phase.

2. Three-Dimensional Electronic Structure and Interband Nesting in the Stoichiometric Superconductor LiFeAs[2)]

Recently discovered iron pnictide superconductors have two-dimensional (2D) Fe–As layers that are similar to the Cu–O planes in high-T_c superconducting cuprates. In high-T_c cuprates, 2D magnetic interaction is important for the origin of the high T_c because of their 2D electronic structure. Such 2D interaction as well as the 2D nesting condition in iron pnictides has long been a focus of discussions. However, the crystal structures of iron pnictides are more three dimensional (3D) than those of cuprates. It is therefore important to clarify the 3D electronic structure of iron pnictides in order to understand the effective interaction of Cooper pair formation.

We reported the electronic structure as well as the orbital characters of a stoichiometric iron-based superconductor LiFeAs (T_c = 18 K) using polarization-dependent 3D angle-resolved photoemission spectroscopy (ARPES) as shown in Figure 2. The obtained band dispersions and orbital characters are qualitatively in good agreement with those derived from local density approximation (LDA) band calculations. Considering a 3D nesting condition, we find that each 2D hole and electron Fermi surface (FS) of d_{xy} orbital character is weakly nested. This weak nesting suggests that (π,π,π) interband scattering is important for the superconducting behavior of LiFeAs.

3. Momentum-Dependent Hybridization Gap and Dispersive In-Gap State of the Kondo Semiconductor SmB_6[3)]

Materials with strong electron correlation have exotic physical properties that cannot be predicted from first-principle band calculations. One example may be seen in a semiconductor with a very small energy gap, which appears in rare-earth compounds such as the Kondo semiconductor or insulator (KI). At high temperatures, KI behaves as a dense Kondo metal, while an energy gap with activation energy of several 10 meV appears at low temperature. The energy gap is believed to originate from hybridization between the nearly localized 4*f* state near the Fermi level (E_F) and the conduction band (*c–f* hybridization).

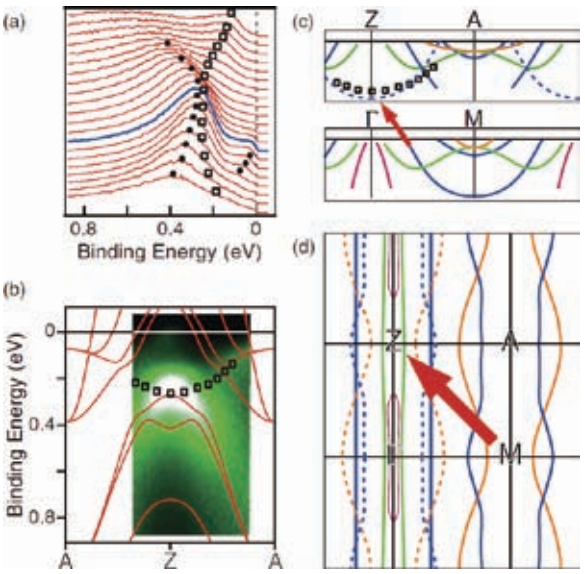

Figure 2. (a)ARPES spectra at the Z point. The solid circles are values that are expected and the open squares are those that are not expected by the band calculation. (b) ARPES image with the band calculation at the Z point. (c) Schematic band dispersions obtained from the experiments. The open squares used in (c) have the same meaning as in (a) and (b). (d) Schematic figure of the 3D FS nesting conditions. The solid and dashed lines indicate the original and nested FSs, respectively. The bold arrow indicates the expected nesting wave vector of (π,π,π).

We reported the temperature dependence of the dispersion curve of the hybridization state using temperature-dependent 3D-ARPES, in order to determine the electronic structure and the reason for the different temperature dependences of the valence transition and magnetic excitation. We found that the hybridization band with a peak at a binding energy of 15 meV near the X point gradually appears on cooling from 150 to 40 K, which has the same temperature dependence as the valence transition. At the Γ point, on the other hand, the peak at E_B ~ 20 meV has the same temperature dependence as the magnetic excitation at Q = (0.5,0.5,0.5), which differs from the 15-meV peak at the X point. This suggests that the magnetic excitation originates from the hybridization band at the Γ point.

References

1) T. Iizuka, T. Mizuno, B. H. Min, Y. S. Kwon and S. Kimura, *J. Phys. Soc. Jpn.* **81**, 043703 (2012). (Papers of Editors' Choice)
2) T. Hajiri, T. Ito, R. Niwa, M. Matsunami, B. H. Min, Y. S. Kwon and S. Kimura, *Phys. Rev. B* **85**, 094509 (2012).
3) H. Miyazaki, T. Hajiri, T. Ito, S. Kunii and S. Kimura, *Phys. Rev. B* **86**, 075105 (2012).

* Present Address; Graduate School of Science, Nagoya University
† Present Address; Physikalisches Institut, Universität Stuttgart, Germany
‡ carrying out graduate research on Cooperative Education Program of IMS with Nagoya University

Electronic Structure and Decay Dynamics in Atoms and Molecules Following Core Hole Creation

UVSOR Facility
Division of Advanced Photochemistry

SHIGEMASA, Eiji — Associate Professor
IWAYAMA, Hiroshi — Assistant Professor
ISHIKAWA, Lisa — Post-Doctoral Fellow

The dynamics of the inner-shell photoexcitation, photoionization, and subsequent decay processes is much more complex, in comparison to outer-shell photo-processes. For instance, the inner-shell photoionization is concomitant with the excitation and ionization of valence electrons, which reveal themselves as shake-up and shake-off satellite structures in the corresponding photoelectron spectrum. The one-photon multi-electron processes, which are entirely due to the electron correlation in the system, are known to happen not only in the primary inner-shell hole creation processes, but also in their relaxation processes. Our research project is focused on elucidating the electronic structures and decay dynamics in core-excited atoms and molecules, by utilizing various spectroscopic techniques together with monochromatized synchrotron radiation in the soft x-ray region.

1. Ultrafast Molecular Dissociation of Core-Excited HBr Studied by High-Resolution Electron Spectroscopy

Soft X-ray absorption spectra of molecules exhibit rich structures in the region below the ionization thresholds, which are due to the excitations of a core electron to unoccupied valence or Rydberg orbitals. The core excited states are predominantly relaxed via Auger electron emission, in the case of the molecules composed of light elements, and subsequently fragmentation follows. As demonstrated by Morin and Nenner, however, a fast neutral dissociation could precede the resonant Auger decay.[1)] In other words, the electronic decay of the core hole takes place after the constituent atoms come apart. Since then, many research works have been conducted to identify such ultrafast dissociation processes in various different systems. Recent works on high-resolution resonant Auger electron spectroscopy have revealed that the nuclear motion of the molecular core-excited states is promoted in competition with the Auger decay. Here, we revisit the first discovery of ultrafast dissociation following the Br 3d core excitation in HBr. High-resolution electron spectroscopy for the subsequent Auger decay has been applied.

The experiments were carried out on the soft X-ray beamline BL6U at UVSOR. The radiation from an undulator was monochromatized by a variable included angle varied line-spacing plane grazing monochromator. The exit slit opening was set to 300 μm, which corresponds to the photon energy resolution $E/\Delta E$ of ~1500 at 70 eV. The monochromatized radiation was introduced into a gas cell with sample gases. Kinetic energies of the emitted electrons were measured by a hemispherical electron energy analyzer (MBS-A1) placed at a right angle relative to the photon beam direction. The degree of the linear polarization of the incident light was essentially 100%, and the direction of the electric vector was set to be parallel to the axis of the electrostatic lens of the analyzer. The energy resolution of the analyzer was set to ~12 meV. Under these experimental conditions, the full width at half maximum of the vibrational fine structure for the X state of HBr^+ was measured to be ~50 meV.

Figure 1 represents a resonant Auger spectrum taken at 70.4 eV, where the $3d_{5/2}$ core-hole states are mainly populated. The vertical scale of the red line spectrum is magnified by the five times. The most marked feature in Figure 1 is the numerous sharp peaks, due to the vibrational structures for the HBr^+ states and the atomic Auger lines from the Br fragments with a 3d core-hole. In the previous work,[1)] only five atomic lines indicated by the blue arrows in Figure 1 have been identified, owing to the limited resolution. In contrast, at least ten more

atomic Auger peaks and some molecular peaks with vibrational structures are clearly resolved in the present work. The detailed analyses for the spectral features observed are just beginning to be performed.

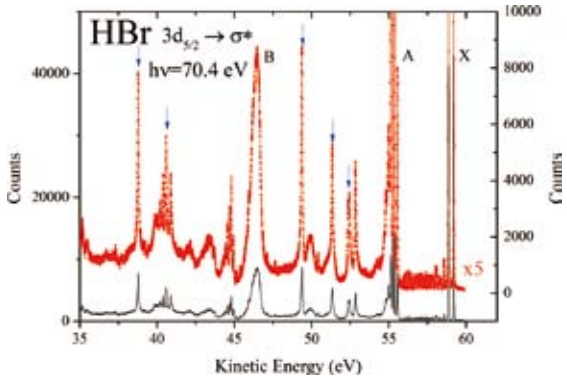

Figure 1. Resonant Auger spectrum taken at the Br $3d_{5/2} \rightarrow \sigma^*$ resonance of HBr.

2. Angle-Resolved Metastable Fragment Yields Spectra

Multi-electron processes, where more than two electrons are excited simultaneously, have usually been observed in absorption and photoelectron spectra of inner-shell excited molecules. Double excitations, one of the typical multielectron processes involving two electrons, are often observed above the ionization threshold energy region in photoabsorption spectra. Shake-up excitations in ions, where one of two electrons is excited into the continuum, are often observed in the energy region close to resonance features in photoelectron spectra. These processes occur mainly due to correlation effects among the electrons in a system and are fundamental aspects of atomic and molecular physics.

Recently, we demonstrated that "metastable" fragments spectroscopy, in which highly excited neutral fragments are observed, is quite useful as a spectroscopic technique for the investigation of multi-electron processes.[2)] Metastable photofragment spectroscopy can also be used for investigating shake-up satellites at the threshold excitation energy, because neutral photofragments can be detected wherever the scanning photon energies match the threshold energies of the ionic states. In addition, if one measures the angular distribution of the fragment emission with respect to the polarization direction of the synchrotron radiation, the symmetries of the inner-shell excited states can be deduced from this information. The angular distribution of fragments emitted after core-hole creation is related to the molecular orientation upon photoabsorption, because the lifetime of the core-hole ($\tau \sim 10^{-14}$ s) is dominated by Auger decay leading to dissociative states and is much shorter than the molecular rotational period ($\tau \sim 10^{-10}$ s). Thus, symmetry-resolved, namely, angle-resolved metastable spectroscopy provides complete symmetry resolution between the $\Delta\Lambda = 0$ (parallel) and $\Delta\Lambda = \pm 1$ (perpendicular) transitions in the *K*-shell photoabsorption of diatomic molecules. As a result, the Σ- or Π-symmetry character of transition states can be detected.[3)]

Figure 2 demonstrates a zero kinetic energy electron (ZEKE) spectrum, and angle-resolved metastable yield spectra of CO in the C *K*-edge region, measured at 0° (Σ-symmetry) and 90° (Π-symmetry), respectively, as an example of successful measurements. The photon energy range shown in Figure 2 corresponds to double and triple excitation regions, where shake-up satellite states also lie. Several peaks are clearly separated by Π-symmetry and Σ-symmetry spectra. We observed new peaks at 310.2 eV, 313.2 eV, and 313.9 eV. These should be double/triple excitation peaks since angle-resolved photoion yield spectra show small peaks at the same energy positions and these peaks have not been observed by conventional photoelectron spectroscopy. We successfully showed that all peaks in angle-resolved metastable fragment yields spectra of CO in the C 1*s* ionization threshold region can be assigned as either satellite states or double/triple excitation states.

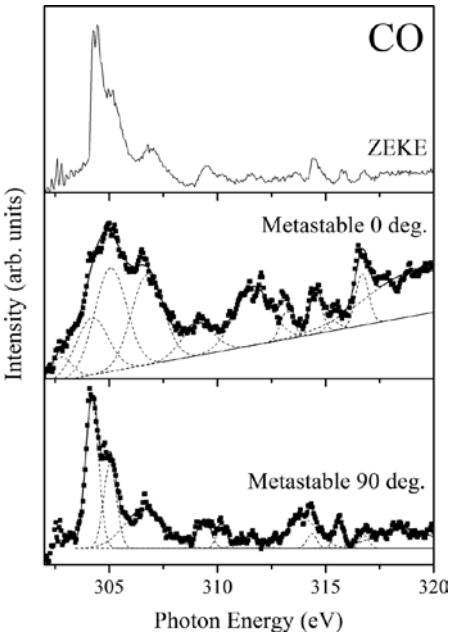

Figure 2. ZEKE spectrum, and angle-resolved metastable yield spectra, measured at 0° (Σ-symmetry) and 90° (Π-symmetry), in the satellite and double/triple excitation regions of CO in the C *K*-edge region.

References

1) P. Morin and I. Nenner, *Phys. Rev. Lett.* **56**, 1913–1916 (1986).
2) Y. Hikosaka *et al.*, *J. Phys. B* **40**, 2091–2097 (2007).
3) E. Shigemasa and N. Kosugi, *Adv. Chem. Phys*. **147**, 75–126 (2012).

Micro Solid-State Photonics

Laser Research Center for Molecular Science
Division of Advanced Laser Development

TAIRA, Takunori	Associate Professor
ISHIZUKI, Hideki	Assistant Professor
AKIYAMA, Jun	IMS Research Assistant Professor
TSUNEKANE, Masaki	Post-Doctoral Fellow
SATO, Yoichi	Post-Doctoral Fellow
KAUSAS, Arvydas	Post-Doctoral Fellow
KONG, Weipeng	Graduate Student
ONO, Yoko	Secretary
INAGAKI, Yayoi	Secretary

The artistic optical devices should be compact, reliable, efficient and high power light sources. With the approaches of domain structures and boundaries engineering, it is possible to bring the new interaction in their coherent radiation. The high-brightness nature of Yb or Nd doped single crystal or ceramic microchip lasers can realize efficient nonlinear wavelength conversion. In addition, designed nonlinear polarization under coherent length level allows us new function, such as the quasi phase matching (QPM). The development of "***Micro Solid-State Photonics***," which is based on the micro domain structure and boundary controlled materials, opens new horizon in the laser science.

1. High Brightness, Passively Q-Switched Yb:YAG/Cr:YAG Micro-Laser

A QCW diode end-pumped, high peak power passively Q-switched Yb:YAG/Cr:YAG micro-laser was demonstrated as shown in Figure 1. An output pulse energy of 3.6 mJ was obtained with a duration of 1.3 ns. The peak power is 2.8 MW. An M^2 value was nearly 1.

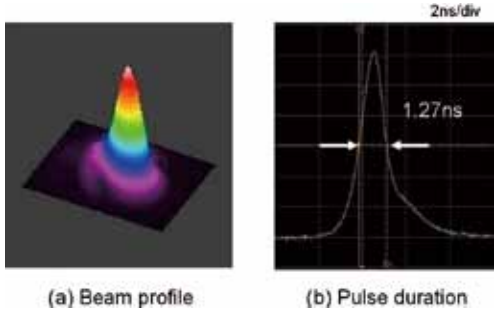

Figure 1. Beam profile and pulse duration at 3.6 mJ.

2. 60% FHG Efficiency from Fluxless-Grown BBO Using Nd:YAG/Cr^{4+}:YAG Microchip Laser

High-efficiency, compact ultra-violet (UV) sources are desirable for many applications, such as, ultrafast UV spectroscopy, photolithography, micromachining, *etc*.

We have developed a Nd:YAG/Cr^{4+}:YAG microchip laser which gives > 8 MW peak power at 100 Hz. We used LBO crystal to obtain 85% second harmonic generation (SHG) and a BBO crystal, grown by a new fluxless method, to obtain 60% fourth harmonic generation (FHG) as shown in Figure 2. A BBO crystal grown by the conventional flux technique can give only 40% FHG under identical conditions. We can obtain a stable pulse train having 3.4 MW peak power with 250 ps pulse width and 100 Hz repetition rate at 266 nm wavelength. We believe that this is the highest conversion efficiency reported so far for the BBO crystal in the generation of deep ultraviolet light.

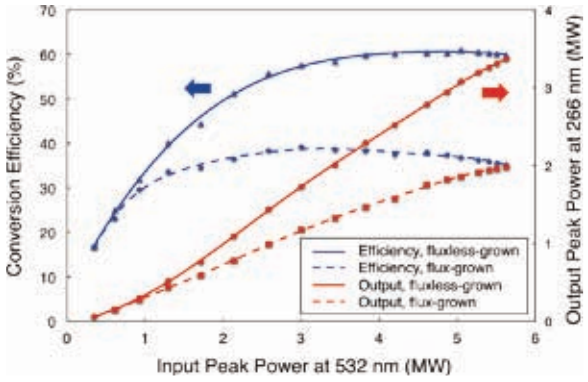

Figure 2. FHG conversion characteristics by different BBO crystal.

3. Lens-Less Edge-Pumped High Power Microchip Laser

A lens-less edge-pumped microchip laser was realized, which is directly pumped by single-emitter diode chips from multiple directions. Figure 3 shows the scheme of this laser head. The lens-less design makes the microchip laser more compact; the multi-direction designable pump schemes can realize desired pump shape. As a preliminary result, continuous wave output power of 32.5 W and slope efficiency of 45% was obtained by 9-direction pumped Yb:YAG ceramic

microchip. Further, 27.2 W single peak Gaussian beam was obtained by a small adjustment of the output mirror. Besides, watt-level high-order Hermite–Gaussian mode, doughnut-shape mode and vortex arrays were demonstrated as an evidence of designable pump scheme. Power scalability is easy by increasing the number of pump diodes to achieve hundred-watt-level high power microchip laser.

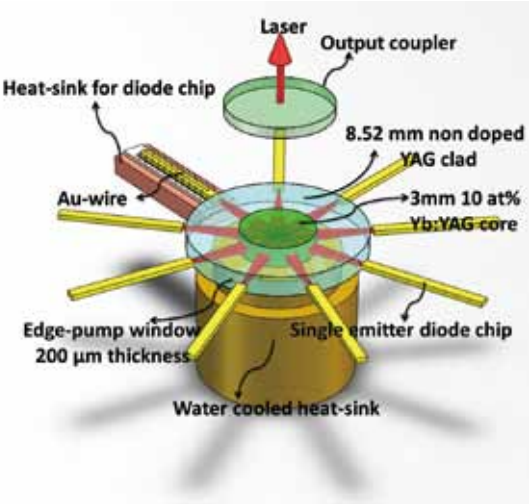

Figure 3. The scheme of lens-less edge-pumped microchip laser.

4. Temperature Dependencies of Stimulated Emission Cross Section for Nd-Doped Solid-State Laser Materials

Temperature dependencies of stimulated emission cross section for Nd:YAG, Nd:YVO_4, and Nd:$GdVO_4$ were carefully evaluated. Our spectral evaluations with fine spectral resolution were carried out under the condition that the population inversion was induced into samples by a weak pumping field. Within the temperature range from 15 °C to 65 °C, the variation of emission cross section at 1.06 μm in Nd:YAG was –0.20%/°C, while those in Nd:YVO_4 and Nd:$GdVO_4$ for π-polarization were –0.50%/°C and –0.48%/°C, respectively. Consideration of measured temperature dependence gave the numerical model for temperature dependent emission cross sections of Nd-doped solid-state laser materials. We have also presented numerical approximations of this model for our samples by a simple polynomial, which can be applicable as shown in Figure 4.

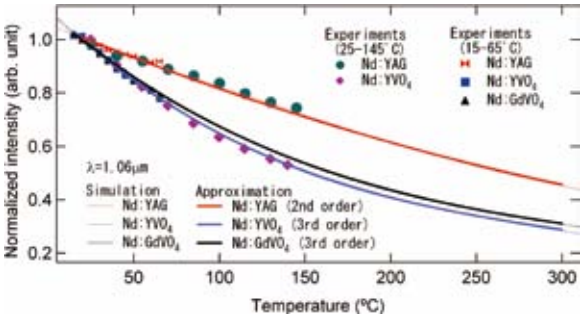

Figure 4. Temperature dependence of emission intensity of various Nd-doped laser media.

5. Fabrication of 10-mm-Thick Periodically Poled Mg-Doped Congruent $LiNbO_3$ Device for High-Energy Wavelength Conversion

Periodically poled Mg-doped congruent $LiNbO_3$ device with 10mm thickness of 32.2 μm period was fabricated by 33 kV pulse application. High-energy optical-parametric oscillation with half-joule-class output energy can be expected by joule-class pumping source in 10 ns pulse region.

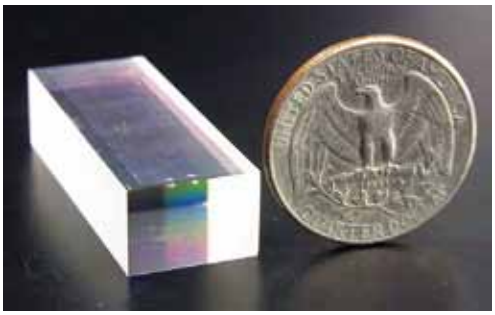

Figure 5. 10-mm-thick PPMgLN device with QPM period Λ = 32.2 μm.

References

1) M. Tsunekane and T. Taira, *The 59th Spring Meeting of the Japan Society of Applied Physics*, 15p-GP6-2 (2012).
2) R. Bhandari and T. Taira, *Opt. Mater. Express* **2**, 914–919 (2012).
3) W. Kong and T. Taira, *Appl. Phys. Lett.* **100**, 141105 (2012).
4) Y. Sato and T. Taira, *Opt. Mater. Express* **2**, 1076 (2012).
5) H. Ishizuki and T. Taira, *Technical Digest of CLEO2012*, CTh1B.1, San Jose, California, USA (May 16–21, 2012).

Ultrafast Laser Science

Laser Research Center for Molecular Science
Division of Advanced Laser Development

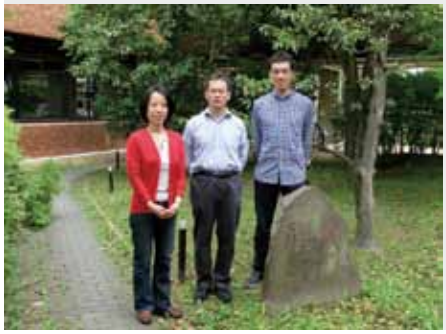

FUJI, Takao — Associate Professor
NOMURA, Yutaka — Assistant Professor
KAWAI, Shigeko — Secretary

Speed of ultrafast energy transfer from light to molecules (*i.e.* primary processes of photosynthesis, photoisomerization in visual pigments, *etc.*) is on the order of femtosecond (10^{-15} s). In our laboratory, we develop cutting edge lasers for such ultrafast molecular science, namely, femtosecond or attosecond (10^{-18} s) ultrashort pulse lasers.

For example, arbitrary waveform synthesis can be perf-ormed with simultaneous generation of femtosecond light pulses in various wavelength regions and superimposition of them with precisely controlled phases.

We would like to develop such advanced light control technology, which can push forward the research on ultrafast photochemical reactions.

1. Generation of Phase-Stable Half-Cycle Mid-Infrared Pulses through Filamentation in Gases[1)]

Filamentation of powerful ultrashort laser pulses in gases is one of the most interesting phenomena in nonlinear optics. The balance between self-focusing and plasma self-defocusing makes the pulse propagate much longer than the Rayleigh range with a very high intensity. It results in a dramatic enhancement of nonlinear processes occurring in the fila-mentation zone. This phenomenon enables high intensity pulse compression and efficient nonlinear wavelength conversion with gas media.

Enhanced nonlinear-optical processes in laser-induced filaments suggest a new strategy for the generation of ultra-short pulses of long-wavelength radiation. Ultrabroadband mid-infrared (MIR, 3–20 μm) pulse generation through fila-mentation in air was firstly demonstrated in 2007,[2)] and the technique was followed by several groups. Such MIR pulses with more than one octave at full width at half maximum are very attractive to be applied for molecular spectroscopy, *e.g.* two-dimensional infrared spectroscopy.

Here we report the latest progress of the ultrabroadband MIR pulse generation through filamentation. By using argon gas as the nonlinear medium and purging the optical path for the MIR pulse with the argon gas, a long tail of the pulse due to free induction decay of atmospheric carbon dioxide and water vapor disappeared, and it was possible to achieve gen-eration of high contrast MIR pulses. Full characterization of the pulse shape of the MIR field indicates that its pulse duration was 7.4 fs, which is about half-cycle period of the center wavelength (3.9 μm) of the pulse.

The experimental setup is shown in Figure 1. The light source was based on a Ti:Sapphire multi-pass amplifier system (Femtolasers, 800 nm, 25 fs, 0.9 mJ at 1 kHz). The second harmonic (ω_2, 25 μJ) and fundamental (ω_1, 675 μJ) pulses were spatially and temporally overlapped and focused into argon by a concave mirror (r = –1000 mm), generating a bright filament with a length of ~3 cm around the beam focus. This filament generated an MIR pulse (ω_0) through an ioni-zation-assisted wave mixing process ($\omega_1 + \omega_1 - \omega_2 \rightarrow \omega_0$). The energy of this MIR pulse was measured as ~250 nJ by using a pyroelectric detector (J-10MB-LE, Coherent). With this energy level, it is possible to apply the pulses for the nonlinear spectroscopy of condensed matter. The pulse-to-pulse intensity fluctuation was about 2.5% rms.

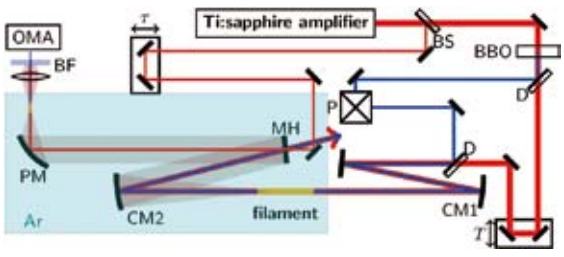

Figure 1. Schematic of the system. The shaded area was purged with argon. BS: beam splitter (5% reflection), BBO: β-BaB_2O_4 crystal (Type 1, θ = 29 deg, t = 0.1 mm), D: Dichroic mirror, P: Periscope, CM1: r = 1 m concave mirror, CM2: r = 0.5 m concave mirror, MH: Aluminium-coated mirror with a hole (ϕ = 7 mm), PM: Aluminium-coated parabolic mirror, BF: Bandpass filter for 335–610 nm (FGB37, Thorlabs), OMA: Spectrometer for ultraviolet region (USB2000+, OceanOptics).

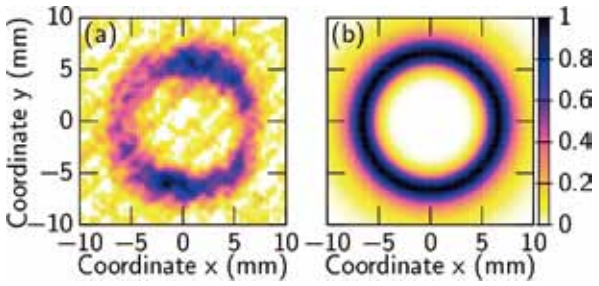

Figure 2. (a) Experimental and (b) simulated radial intensity distributions of the mid-infrared pulses.

The beam profile of the MIR beam after ZnSe and Si filters measured with a pyroelectric camera (Pyrocam III, Spiricon) is shown in Figure 2(a). The shape of the beam was ring and the angle of the cone was estimated to be about 3 deg. Some asymmetric shape and distortion from ideal ring pattern comes from residual pulse front tilt and/or astigmatism of the light source. The generated MIR pulse has basically pure one-direction linear polarization (>40:1) in the entire cross-section of the beam as the input pulses, which fact was confirmed with a wire grid polarizer (NT62-774, Edmund).

We compare the experimental result with FWM-beam analysis based on a straightforward integration of the FWM response over the beam overlap region. As can be seen from Figure 2(b), the simple approach provides an accurate agreement with the experimental result. It confirms that the ring-shaped beam profile originates from a dramatic confocal-parameter mismatch between the MIR field and the laser beams.

Additionally, the ~12 mm diameter beam was focused down to 1.0 mm with a r = 2 m concave mirror, indicating a reasonable focusability for a ring shaped spatial mode. The beam profile at the focal point. Although the beam may contain some angular dispersion, the dispersion is basically radially symmetric, and thus does not significantly deteriorate the good focusability of our MIR beam.

In order to quantitatively evaluate the temporal shape of the generated MIR pulse, we measured cross-correlation frequency-resolved optical gating (XFROG) We used argon again as a nonlinear medium and used four-wave mixing process ($\omega_1 + \omega_1 - \omega_0 \rightarrow \omega_2$) as a nonlinear interaction between the test pulse (MIR pulse) and the reference pulse. The scheme is free from spectral filtering caused by phase matching condition in the nonlinear interaction.

The system for the XFROG measurement is also shown in Figure 1. Small portion (~2 μJ) of the fundamental 25-fs pulse was used as a reference pulse. The reference pulse and the MIR pulse (test pulse) were combined through a mirror with a hole and focused into argon with an aluminium-coated parabolic mirror (f = 150 mm). Generated blue spectra (centered around 440 nm) were measured with a spectrometer (USB 2000+, OceanOptics) by scanning the delay time (τ in Figure 1) between the reference pulse and the MIR test pulse.

The measured and the retrieved XFROG traces are shown

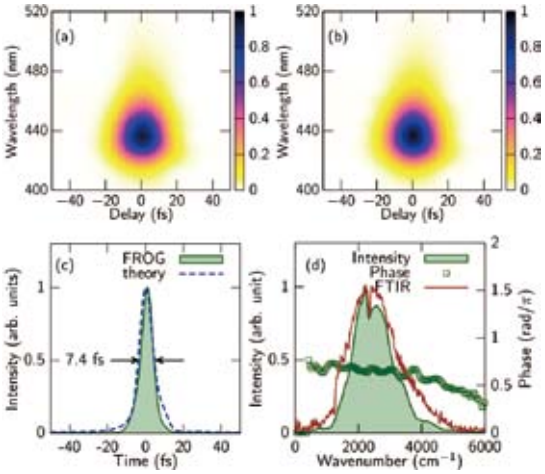

Figure 3. (a) Experimental and (b) retrieved XFROG traces. The retrieved pulse in (c) time and (d) frequency domain. The temporal profile from the 3D numerical simulation and the spectrum measured with Fourier transform spectrometer are also shown. Measured XFROG trace.

in Figure 2(a) and (b). The main feature of the trace indicates that the residual chirp of the test pulse is very small. The FROG error was 0.0009 with 256 × 256 grid. The retrieved time and frequency domain pictures are shown in Figure 2(c) and (d), respectively. The pulse width is estimated to be 7.4 fs, which is 0.57 cycles for 3.9 μm carrier wavelength. The retrieved spectrum is spread over whole MIR region (500–5000 cm^{-1}). The broadness of the spectrum was due to the weak dispersion of the medium, with the phase-matching length exceeding the length of the filament for all the MIR spectral components observed in the experiments.

In conclusion, ultrabroadband coherent MIR spectrum which covers the entire MIR region was generated through two-color filamentation. Due to the spatial and temporal quality, ultrashort MIR pulses generated in two-color filaments are ideal for numerous applications. In our experiments, MIR pulses as short as 7.4 fs were generated, which corresponds to about a half-cycle of 3.9 μm center wavelength.

The light source has a potential to change the situation of traditional MIR spectroscopy dramatically. For example, the coherent broadband MIR light source enables us to obtain absorption spectra through entire MIR region by single-shot with chirped pulse up-conversion technique. The reasonable quality of the spatial mode can be useful for efficient MIR microscope imaging combined with the up-conversion technique. Multi-dimensional spectroscopy for entire MIR region to monitor vibrational coupling among very different vibrational modes can be realized with the light source.

References

1) T. Fuji and Y. Nomura, *21th International Laser Physics Workshop (LPHYS'12)*, 5.2.1 Calgary, July 23–27 (2012). (invited talk)

2) T. Fuji and T. Suzuki, *Opt. Lett.* **32**, 3330–3332 (2007).

Visiting Professors

Visiting Professor
KONDOH, Hiroshi *(from Keio University)*

Surface Dynamic Processes Studied by Soft X-Ray Spectroscopy

Surface physics and surface chemistry have made significant progress in understanding of surface static structures but much less progress has been made with respect to understanding of surface dynamic processes. We have been interested in surface dynamic processes such as catalytic reactions at surfaces of metals and oxides. Recently we have been working on oxide photocatalysts using synchrotron radiation in a soft-x-ray region. In particular, we studied the geometric and electronic structures of N-doped TiO_2 at BL3U and BL6U in the UVSORII and determined the local structure of the doped nitrogen that induces the visible-light response of the photocatalyst. Another research subject concerns understanding of catalytic reactions on metal nanoparticles which proceed under practical working conditions. A soft x-ray absorption spectroscopy with the transmission mode has been developed at BL3U in such a way that real-time observations of catalytic processes under gas flow with ambient-pressure conditions can be conducted. Catalytic reactions over metal nanoparticles that are enhanced by absorption of the gas molecules inside the particles will be studied with this technique.

Visiting Professor
NODA, Susumu *(from Kyoto University)*

Strong Coupling of Single Atoms to Photonic Crystal Cavity Field

We have investigated photonic crystal structures which enable modification of propagation properties of an electromagnetic field and also tight confinement of the field to a tiny resonator. Accordingly the field strength inside the resonator is much enhanced and therefore the field can be strongly coupled to a quantum emitter such as a quantum dot even at a single photon level. Such a nanostructure device would be suitable for applications in optical communication and future quantum information processing in terms of its scalability. We have studied the strong coupling of the cavity field with a quantum dot and also the Purcell effect. Recently we have been interested in adopting a single cold atom as a quantum emitter, which shows much longer coherence time and therefore would be desirable for future application. Cold atoms are first loaded into a magneto-optical trap and then one of them is captured in tightly-focused optical tweezers. A movable lens-positioner can translate the position of the focal point, thereby transferring the trapped atom to the vicinity of the photonic crystal cavity. With this technique, the strong coupling of the single atom with the cavity field will be studied.

Visiting Professor
ITO, Atsushi *(from Tokai University)*

X-Ray Spectromicroscopy of Biomedical Specimens

Soft X-ray microscopy has a great advantage over other microscopies in the mapping of light elements or molecules containing such elements at high resolution. The mapping is realized by X-ray spectromicroscopy which utilizes unique spectral features of elements and molecules, that is, absorption edges and XANES profiles observed in the vicinity of the absorption edge. Our effort to apply spectromicroscopy to biomedical specimens has been focused on the mapping of sulfur oxidation state in human hair, because hair consists of mainly cystine, a sulfur-rich amino acid. Cystine is oxidized to cysteic acid by oxidative damage. Both products were found to have significantly different XANES peaks at the S-K absorption edge. Spectromicroscopy in combination with an electronic zooming tube as a two dimensional detector revealed that the oxidative damage was preferentially generated in the outer part of hair called cuticle. Furthermore a bleaching treatment of hair also increased the content of cysteic acid.

Visiting Associate Professor
TSUBOUCHI, Masaaki *(from Japan Atomic Energy Agency)*

Development of THz Tomography of Photo-Induced Carrier

We are developing a new technique for the THz tomography of photo-induced carriers in a semi-conductor based on the optical-pump THz-probe reflection spectroscopy. Since the photo-induced carrier strongly interacts with the THz light, the measurement and control of the carrier distribution and dynamics are significantly important to design THz optics using semi-conductors. Our THz tomography is a noncontact technique which determines both the dynamics and the spatial distribution of photo-induced carrier, simultaneously. We are demonstrating the THz tomography using photo-excited silicon (Si), and comparing the experimental results with the exact solutions of Maxwell's equations.